

# A novel structural design of air cathodes expanding three-phase reaction interfaces for zinc-air batteries

Lyuming Pan<sup>a,b,c</sup>, Dongfang Chen<sup>a,b,\*</sup>, Pucheng Pei<sup>a,b,\*</sup>, Shangwei Huang<sup>a,b</sup>, Peng Ren<sup>a,b</sup>, Xin Song<sup>a,b</sup>

<sup>a</sup> State Key Lab. of Automotive Safety and Energy, Tsinghua University, Beijing 100084, China

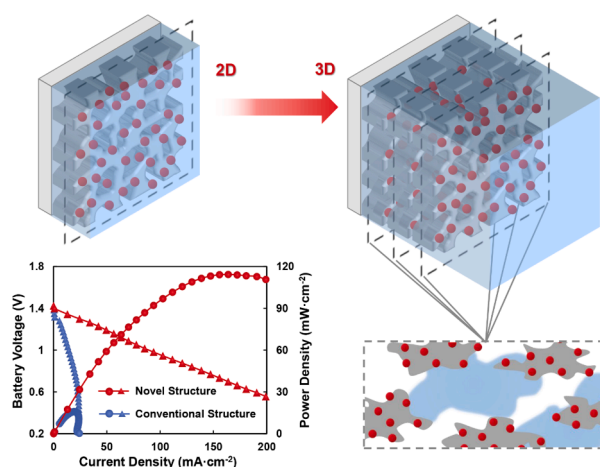
<sup>b</sup> School of Vehicle and Mobility, Tsinghua University, Beijing 100084, China

<sup>c</sup> Tsinghua Shenzhen International Graduate School, Tsinghua University, Shenzhen 518055, China

## HIGHLIGHTS

- The three-phase reaction interfaces expand from 2D plane to 3D zone.
- The power density increases by using novel structure.
- A peak power density of  $120 \text{ mW}\cdot\text{cm}^{-2}$  for zinc-air battery is achieved.
- Performance decay of air cathodes isn't obvious after continuous discharging.

## GRAPHICAL ABSTRACT



## ARTICLE INFO

### Keywords:

Zinc-air batteries  
Air cathodes  
Structural design  
Three-phase reaction interfaces  
Hydrophobicity adjustment

## ABSTRACT

Zinc-air batteries are considered as potential energy conversion systems. One of the main issues of zinc-air batteries is the low actual power density. However, the three-phase reaction interfaces are limited in 2D plane of conventional air cathodes, which limits the electrochemical kinetics and the commercialization of zinc-air batteries. Here, a novel structural design of air cathodes with multi current collectors and gradient hydrophobicity to improve the discharge power for zinc-air batteries is proposed. Based on non-noble metal catalysts, the three-phase reaction interfaces expand from 2D plane to 3D zone by the novel structural design, increasing the power density of the battery. The gradient distribution of hydrophobicity in the air cathode can be obtained in one step through the soaking-drying process. When the soaking-drying process reaches twice, the optimal performance is achieved due to the balance of hydrophilicity and hydrophobicity. The peak power density of  $120 \text{ mW}\cdot\text{cm}^{-2}$  is achieved in the zinc-air battery with  $\text{MnO}_2$  as catalysts. After continuously discharging at 20

\* Corresponding authors at: State Key Lab. of Automotive Safety and Energy, Tsinghua University, Beijing 100084, China.

E-mail addresses: [dfchen@mail.tsinghua.edu.cn](mailto:dfchen@mail.tsinghua.edu.cn) (D. Chen), [pchpei@mail.tsinghua.edu.cn](mailto:pchpei@mail.tsinghua.edu.cn) (P. Pei).

<https://doi.org/10.1016/j.apenergy.2021.116777>

Received 25 October 2020; Received in revised form 9 February 2021; Accepted 3 March 2021

Available online 16 March 2021

0306-2619/© 2021 Elsevier Ltd. All rights reserved.

$\text{mA}\cdot\text{cm}^{-2}$  exceed 9 h, the electrochemical performance can be restored by replacing with a new metal anode and keeping the initial air cathode. This work illustrates that the novel structural design of air cathodes can effectively improve the power density of zinc-air batteries, which is beneficial to the application of zinc-air batteries in the fields of energy storage and conversion.

## 1. Introduction

With the increase of both fossil energy consumption and environmental pollution, more environment-friendly energy conversion systems are called for to satisfy the demand for industrial production and daily life [1,2]. Due to the high theoretical specific energy, safety, environmental friendliness, and low cost, metal-air batteries have drawn much research interests in recent years [3,4], whose anode material is usually lithium, zinc, or other metals that can be produced efficiently in the developed metallurgical and manufacturing industry. When air is used as the cathode material in the battery system, an additional auxiliary gas storage tank is unnecessary [5–7]. The electrolyte between anode and cathode can be used not only to transport and store charged particles but also to recover anode materials through metal ions. Compared to lithium and aluminum, zinc is more affluent in nature, lower in cost, and more moderate in chemical activities [8]. These characteristics enable zinc-air batteries to utilize aqueous solutions as the electrolytes directly, which not only makes the reaction process safer but also avoids the consumption of the metal due to severe corrosion reaction in the solution. Therefore, zinc-air batteries are considered as potential energy conversion systems especially as backup energy, power system and wearable devices [9–11].

At present, the main problems of zinc-air batteries are low specific energy, low power density, and short cycle life [12–14], which are closely related to the air cathode. In order to solve these problems, the air cathode need to meet the following conditions: (1) effectively catalyze chemical reactions [15–17]; (2) build smooth mass transfer channels [18,19]; (3) form fast charge transfer channels [20,21]; (4) maintain the stability of catalysis, mass transfer and charge transfer performance [4,22]; (5) lower the production cost [8,23]. In order to meet these conditions, the conventional structure of air cathodes has been widely reported [20,24]. However, based on the conventional air cathodes, it is difficult to improve the output power of zinc-air batteries, which needs to synthesize catalysts with large specific surface area and high catalytic kinetics. The conventional structure of air cathodes consists of a current collector, a hydrophobic diffusion layer and a catalytic layer (Fig. 1a). The catalytic layer is tightly coated on the surface of the current collector, and the three-phase reaction interfaces is formed on its active area, which is a two-dimensional (2D) plane. When the superficial area of the air cathode is fixed, the expansion of the three-phase reaction interfaces depends on the catalyst with large amount of micro pores and large specific surface area (Fig. 1b). The expansion of the catalyst surface area increases its contact with electrolyte and air, and the existence of porous structure is conducive to the balance of liquid and gas phase,

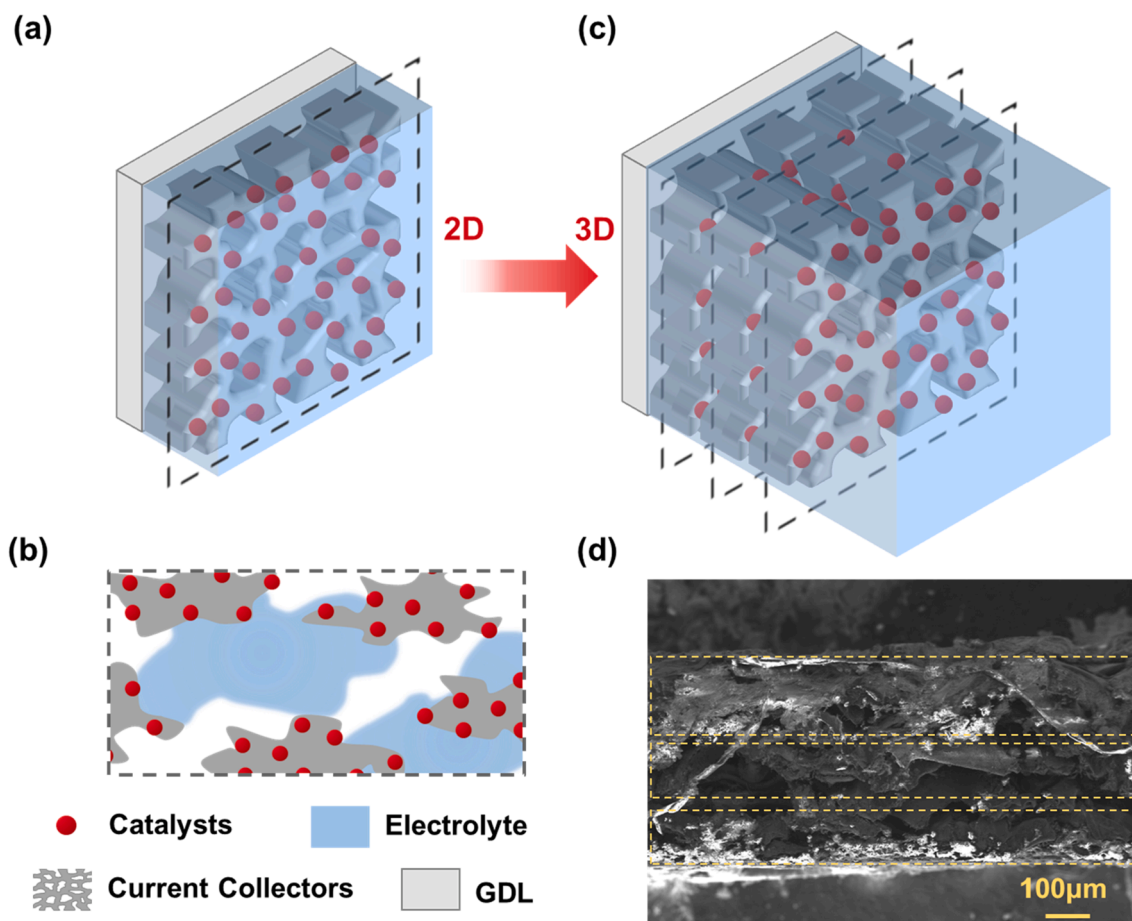


**Fig. 1.** Comparison of different air cathode structures. The schematic diagram of (a) the structure of conventional air cathodes, (b) three-phase reaction interfaces, (c) the novel structure of air cathodes with multi current collectors and (d) the corresponding SEM image.

which helps to form the three-phase reaction interfaces. In addition, the catalytic activity of the catalyst has a significant impact. There are reports [25–27] on catalysts focusing on the efficiency of oxygen reduction and oxygen evolution, good conductivity, low cost and so on. However, the development of catalysts based on the conventional structure usually requires complex preparation process to obtain catalysts with special composition and structure. The fundamental reason is that the three-phase reaction interfaces is formed in the 2D plane of the catalytic layer in the conventional air cathodes, which is difficult to increase further. Therefore, a novel structural design of air cathodes is needed to avoid the complex and expensive catalyst preparation for low-cost and high-power output zinc-air batteries that is suitable for commercial applications.

The optimization of air cathodes mainly focuses on the hydrophobicity adjustment based on the conventional structure in existing researches. Hydrophobicity can directly determine the relative dominance of electrolyte and air, so it affects the formation of the three-phase reaction interfaces and determines the mass transfer rate during the oxygen reduction reaction (ORR) process. The construction of the three-phase reaction interfaces is related to the hydrophobicity of air cathodes [11,25,26]. When the electrolyte and air balance each other, the three-phase reaction interfaces is easier to form [28]. The regulation of hydrophobicity can be achieved by controlling the distribution of hydrophobic materials. Shen et al. [29] soaked carbon papers with different concentrations of poly(tetrafluoroethylene) (PTFE) emulsion (10%, 20%, 30%, 40%) and then calcined at high temperature. The hydrophobicity of treated carbon papers was enhanced in turn, which was used as the air cathode of lithium-air batteries together with the same catalysts. In the same specific capacity range, it was found that the discharge voltage of lithium-air batteries corresponding to the 30% PTFE emulsion was the highest. In addition, the hydrophobicity can be adjusted by changing the treatment times. Ni et al. [30] directly grow  $\text{Co}_3\text{O}_4$  nanosheets on nickel foam. After soaking in the same concentration of PTFE emulsion for 1, 2, and 4 times separately, the hydrophobicity of the nickel foam increased sequentially. The assembled zinc-air / zinc- $\text{Co}_3\text{O}_4$  hybrid batteries with air cathodes, which was treated for two times in the PTFE emulsion, showed the highest discharge voltage and power density. The air cathode with in-situ growth catalysts should be moderately hydrophobic. The adjustment of hydrophobicity can be assisted by carbon materials. Wang et al. [31] prepared nickel foam directly growing  $\text{MnO}_2$  nanosheets. The air cathodes were obtained by the hydrothermal reaction in an emulsion containing different concentrations of PTFE and carbon nanotube (CNT). Zinc-air batteries equipped with air cathode containing CNT had lower load transfer impedance and higher discharge voltage.

It has been proved that it is effective to adjust the hydrophobicity for constructing the three-phase reaction interfaces and optimizing the mass transfer in air cathodes. However, it is limited to increase the discharge power density of zinc-air batteries only by optimizing the hydrophobicity in the conventional air cathodes. Therefore, it is urgent to develop a novel structure which can expand the area of the three-phase reaction interfaces efficiently and easily, and then improve the power output of zinc air batteries.

Herein, a novel air cathode structural design is proposed and verified to improve the power density of zinc-air batteries. The novel structural design includes multi current collectors with in-situ growth catalysts, gradient distribution hydrophobic materials (PTFE), and a gas diffusion layer on the outside (Fig. 1c, d). The novel structure expands the three-phase reaction interfaces from 2D plane to three-dimensional (3D) zone. Based on the existing cheap catalysts instead of complex and expensive catalysts, the complex synthesis process can be eliminated and the output power of zinc-air batteries can be effectively increased. In the validation experiments,  $\text{MnO}_2$  nanosheets were directly grown on nickel foam as catalysts and current collectors by a one-step hydrothermal reaction. By keeping the upper and lower positions of nickel foam unchanged during the subsequent soaking-drying process, the gradient

distribution of hydrophobic materials in the air cathode is easily controlled. With  $\text{MnO}_2$  as the catalysts, the peak power density of zinc-air batteries can reach  $120 \text{ mW}\cdot\text{cm}^{-2}$  by using this novel air cathode structure. In this paper, the effect of hydrophobicity and the number of current collectors on the performance of air cathodes is evaluated. Through adopting appropriate parameters, the power density of zinc-air batteries is significantly increased.

## 2. Experimental

### 2.1. Synthesis of $\text{MnO}_2$ nanosheets in-situ grown on nickel foam ( $\text{MnO}_2/\text{NiF}$ )

All chemical reagents were of analytical purity and utilized without any further purification. The  $\text{MnO}_2/\text{NiF}$  was fabricated by a hydrothermal reaction, as previously reported [32]. Briefly, the nickel foam ( $15 \text{ mm} \times 40 \text{ mm}$ , 3-mm thickness, Shenzhen Lifeixin Environmental Protection Co., Ltd) was soaked in 3 M HCl (Beijing Chemical Factory), followed by ultrasonic treatment of 10 min to remove the surface oxide layer. Then rinsed them with deionized water three times. Place one piece of nickel foam at the bottom of a 50-mL Teflon-lined autoclave containing a homogenous solution of  $\text{KMnO}_4$  (0.2 g, Beijing Tongguang Fine Chemical Co., Ltd.) in 20 mL of deionized water. After reaction at  $180^\circ\text{C}$  for 8 h, the substrates coated with  $\text{MnO}_2$  nanosheets were removed and immersed in ethanol and deionized water (volume ratio 1:4) for 12 h, and finally washed with deionized water under ultrasound for 20 mins to remove physisorbed and loosely attached  $\text{MnO}_2$ , followed by drying at  $60^\circ\text{C}$  overnight. The loading of  $\text{MnO}_2$  was calculated to be approximately  $0.2 \text{ mg cm}^{-2}$ .

### 2.2. Fabrication of $\text{MnO}_2/\text{NiF}$ air cathode

The air cathodes were fabricated by a soaking-drying process and two hot-pressing processes. During a hot-pressing process, different number of  $\text{MnO}_2/\text{NiF}$  (1–5 pieces) were overlapped each other and pressed three times under a pressure of 30 MPa by the hot press (Shenzhen Xotech Technology Co., Ltd., TH-XC605-HC200) with the surface temperature at  $80^\circ\text{C}$ . Different thickness (0.3 mm, 0.6 mm, 0.9 mm, 1.2 mm, 1.5 mm) was obtained. To furnish a hydrophobic surface that facilitates oxygen diffusion, the  $\text{MnO}_2/\text{NiF}$  were coated with PTFE by a 1 min soaking in PTFE emulsion (5 wt%, Shanghai Hesen Electric Co., Ltd) and drying at  $60^\circ\text{C}$  for 20 min, which is a typical soaking-drying process. To change the surface hydrophobicity, different soaking-drying times (from 0 to 3 times) were applied. Then, the samples were annealed at  $300^\circ\text{C}$  in the air for 1 h at a heating rate of  $5^\circ\text{C}\cdot\text{min}^{-1}$ . Finally, the  $\text{MnO}_2/\text{NiF}$  electrodes were coated with a gas diffusion layer (QuantumSphere Inc.) followed by another hot-pressing process under the same conditions. The resultant samples were denoted as  $\text{MnO}_2/\text{NiF} \times \chi\text{-PTFE-}\gamma$ .  $\chi$  represents the number of  $\text{MnO}_2/\text{NiF}$  piece, and  $\gamma$  represents the soaking-drying treatment times.

### 2.3. Materials characterization

The morphological investigation was performed using scanning electron microscopy (SEM, Merlin, Carl Zeiss, Germany) at 5 kV accelerating voltage. The chemical compositions of the electrodes were determined by energy-dispersive X-ray spectroscopy (EDS, Merlin, Carl Zeiss, Germany) at an accelerating voltage of 15 kV, and X-ray diffraction (XRD, Bruker D8 Advance, Bruker, Germany) was adopted to analyze the crystal structure of the catalysts with continuous scanning in the diffraction angle range ( $2\theta$ ) of  $10\text{--}80^\circ$  with  $\text{Cu K}\alpha$  source working at 40 keV. X-ray photoelectron spectroscopy (XPS) was performed on an ESCALAB 250Xi (Thermo Fisher, England) using  $\text{Al K}\alpha$  radiation as the radiation source. All the binding energies are referenced to the  $\text{C1s}$  peak at 284.8 eV. The hydrophobicity of different electrode surfaces was characterized by a contact angle measurement system (Attention Theta

Lite).

#### 2.4. Assembly and test of zinc-air batteries

The zinc-air battery was composed of the as-prepared air cathode, a polished zinc foil (0.2 mm, Qizhou Gaogang Diaopu Optical Co., Ltd.) as the anode, and 6 M KOH (Modern Oriental Technology Development Co., Ltd) + 0.2 M ZnO (Tianjin Zhiyuan Chemical Reagent Co., Ltd.) as the electrolyte. The geometric area of the cathode exposed to air was approximately 1 cm<sup>2</sup>, and the same area of the catalyst layer was exposed to the electrolyte. The battery voltage at the current step of 1 mA s<sup>-1</sup> was recorded to get the polarization curves. Constant current discharge measurements were conducted to evaluate the discharge performance. The electrochemical workstation (VersaSTAT 3F, Princeton Applied Research) was utilized for the measurements. The power density of zinc air battery is calculated by the following formula:

$$\text{power density} = \frac{\text{battery voltage} \times \text{battery current}}{\text{active surface area}}$$

### 3. Results and discussion

#### 3.1. Morphology, crystal structure, and chemical composition

In order to verify the advantages of the novel air cathode structural design, MnO<sub>2</sub> was selected as the electrocatalyst. MnO<sub>2</sub> has many crystal structures. Among them, δ-MnO<sub>2</sub> showed excellent ORR catalytic activity [33]. In addition, δ-MnO<sub>2</sub> can be obtained by a simple one-step hydrothermal reaction without additional pH adjustment [34]. Therefore, δ-MnO<sub>2</sub> grown on nickel foam is a reasonable choice. SEM images and EDS elemental mappings are shown in Fig. 2. The pristine nickel foam (Fig. 2a) indicates a porous structure composed of nickel skeleton with macropores. After the hydrothermal reaction, the vertical MnO<sub>2</sub> nanosheets on nickel foam (Fig. 2b) are observed. The inset in Fig. 2b presents magnified SEM images of MnO<sub>2</sub>/NiF, further revealing its microstructures. The hierarchical macroporosity of the pristine nickel foam is still observed with MnO<sub>2</sub> nanosheets thoroughly and generally distributing on the nickel skeleton structure. The length of the

nanosheets typically varies between 0.5 μm and 1 μm. The crystal nanosheets are composed of mesopores, which are favorable for mass transport. The so-called MnO<sub>2</sub> nanosheets are two-dimensional materials, and it can wholly and uniformly cover the three-dimensional net of foamed nickel. This structure provides good transport characteristics for the electrode in the process of O<sub>2</sub> diffusion. It promotes the transport of ions in the chemical reaction [24], which is conducive to the realization of high catalytic active site utilization and the increase of catalytic activity area. The MnO<sub>2</sub> on the nickel foam contains Ni, Mn, and O as the main chemical elements according to the EDS analysis (Fig. 2c). A clear nickel foam structure can be observed from EDS images of Mn, O and Ni elements. This shows that these elements have a relatively homogeneous distribution throughout the entire region. After the soaking-drying process, the back of MnO<sub>2</sub>/NiF is covered with PTFE (Fig. 2d), which will be beneficial to improve the hydrophobicity. With PTFE covering, the macropores of MnO<sub>2</sub>/NiF are retained at the backside throughout the layer. The backside is attacked with gas diffusion layer (GDL) to provide a mass transport property for the diffusion of O<sub>2</sub> and facilitated ion diffusion during the catalytic process.

The XRD patterns from 10° to 80° of nickel foam and MnO<sub>2</sub>/NiF are presented in Fig. 3a. For both samples, the intense peaks of nickel can be clearly observed. Diffraction peaks were detected for MnO<sub>2</sub> at 14.1°, 22.4°, 29.5°, 38.7° and 45.0°, which could be separately assigned to the (001), (002), (200), (-111) and (-112) planes of the birnessite-type manganese oxide nanosheets (JCPDS 80-1098). The characteristic peak of δ-MnO<sub>2</sub> is lower than that of Ni because the loading of catalysts is very small (0.2 mg·cm<sup>-2</sup>). In addition, no other characteristic peaks were clearly observed. This indicates that the main component of the crystal is δ-MnO<sub>2</sub>. This result confirms the successful synthesis of the reported structure for δ-MnO<sub>2</sub> on nickel foam [32]. XPS was employed to analyze the chemical states of Mn and O on the electrode surface. Fig. 3b elucidates the identical XPS spectra of MnO<sub>2</sub>/NiF. The presence of manganese oxide is evidenced by manganese Mn 2p peaks and oxygen O 1s peaks [35]. As illustrated in Fig. 3c, the Mn 2p region consists of a spin-orbit doublet of Mn 2p<sub>1/2</sub> and Mn 2p<sub>3/2</sub> with the binding energy of 653.8 eV and 642.2 eV, respectively. Mn 2p<sub>1/2</sub> and Mn 2p<sub>3/2</sub> can be deconvoluted at 654.6, 653.7, 643.2, and 642.2 eV, which are attributed

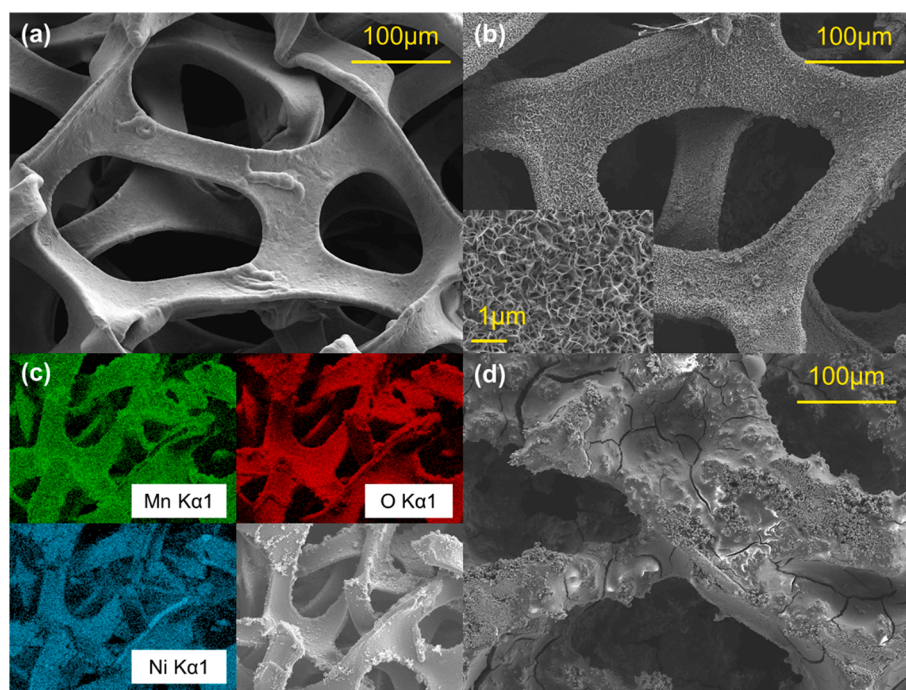


**Fig. 2.** SEM images of (a) Ni foam and (b) MnO<sub>2</sub>/NiF. (c) The EDS elemental mappings of the corresponding elemental. (d) SEM image of MnO<sub>2</sub>/NiF covered with PTFE.

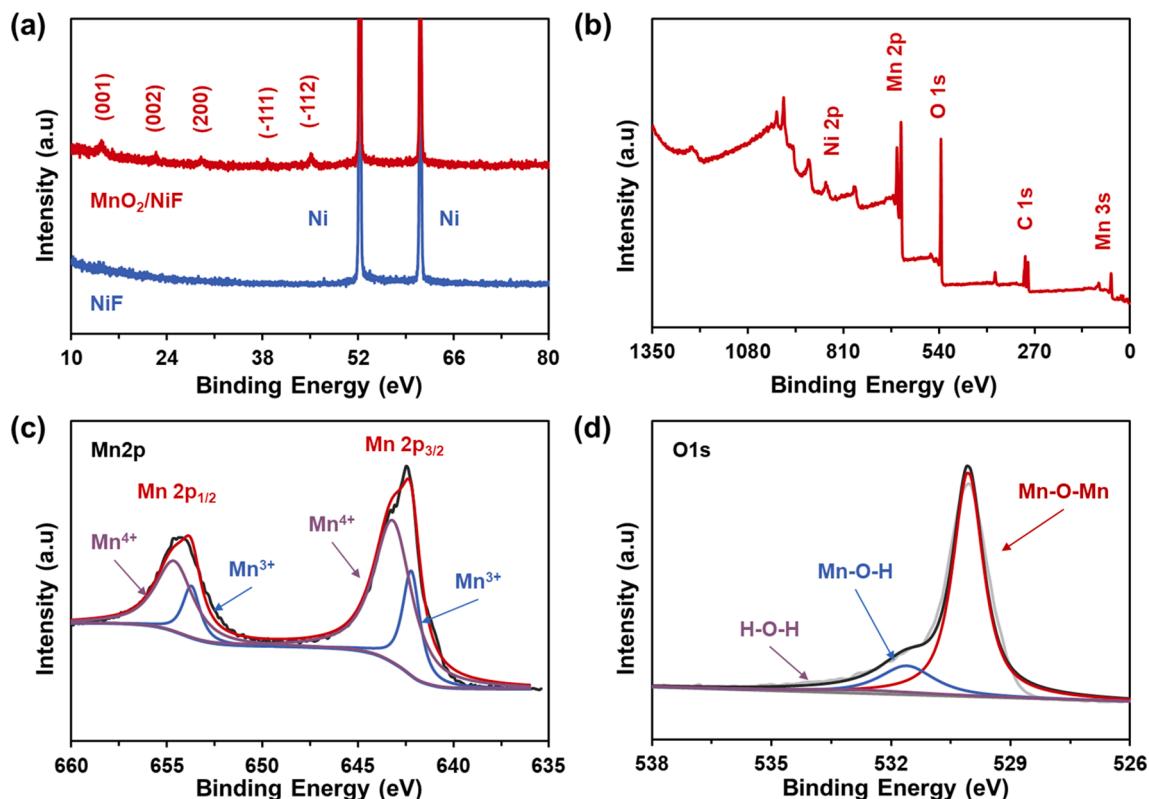


**Fig 3.** (a) XRD patterns of nickel foam and MnO<sub>2</sub>/NiF; (b) Surface scanning XPS spectra of MnO<sub>2</sub>/NiF; (c) Mn 2p and (d) O1s core level XPS spectra with deconvoluted peaks for MnO<sub>2</sub>/NiF.

to the presence of Mn<sup>4+</sup> and Mn<sup>3+</sup> oxide phases, respectively. For the deconvoluted results of Mn2p in XPS, the proportions of Mn<sup>3+</sup> and Mn<sup>4+</sup> are calculated by the following formula respectively.

$$P(\text{Mn}^{3+}) = \frac{S_{\text{Mn}^{3+}}}{S_{\text{Mn}^{3+}} + S_{\text{Mn}^{4+}}} \times 100\%$$

$$P(\text{Mn}^{4+}) = \frac{S_{\text{Mn}^{4+}}}{S_{\text{Mn}^{3+}} + S_{\text{Mn}^{4+}}} \times 100\%$$

where  $S_{\text{Mn}^{3+}}$  and  $S_{\text{Mn}^{4+}}$  represents the contribution from Mn<sup>3+</sup> and Mn<sup>4+</sup>, respectively. And the amount of Mn<sup>4+</sup> and Mn<sup>3+</sup> oxide phases is determined to be 74.4% and 25.6%, respectively. The results indicate the dominated oxidation state of the mixed-valence manganese oxides is tetravalent [36]. The presence of Mn<sup>3+</sup> leads to rich oxygen defects in the materials, which can make better electrocatalytic performance [37]. The existence of manganese oxide phases is also reflected in the O1s spectra shown in Fig. 3d. The two sharp peaks at 530.1 and 531.6 eV are attributed to the oxygen atoms bound to Mn atoms represented by Mn—O—Mn of the tetravalent oxide and Mn—O—H bond of a hydroxide, respectively. The broad peak at 532.9 eV is corresponding to H—O—H bond of residual water. The average oxidation state of Mn is calculated as follows[31,38]

$$\text{Mn State} = \frac{4 \times (S_{\text{Mn-O-Mn}} - S_{\text{Mn-O-H}}) + 3 \times S_{\text{Mn-O-Mn}}}{S_{\text{Mn-O-Mn}}}$$

where  $S_{\text{Mn-O-Mn}}$  represents the contribution from both MnOOH and MnO<sub>2</sub>, whereas  $S_{\text{Mn-O-H}}$  stands for the contribution from hydroxyl groups.

According to the intensities of the Mn—O—Mn and Mn—O—H components, quantitative calculations illustrate that the average oxidation state of Mn is 3.78, which is consistent with the deconvoluted results of Mn2p.

### 3.2. Effect of surface hydrophobicity on battery performance

For the air cathode, not only the catalytic active materials loading but also the surface hydrophobicity is the critical factor for the discharge performance of zinc-air batteries. For the oxygen reduction reaction in the zinc-air battery, the hydrophobicity is needed for increasing the three-phase reaction interfaces. The object of the soaking-drying process of MnO<sub>2</sub>/NiF with PTFE emulsion is to increase its hydrophobicity. As previously reported [39,40], a gradient distribution of hydrophobic materials throughout the air cathodes is conducive to three-phase reaction interfaces constructed formation, which requires multiple waterproof treatments to obtain gradient hydrophobicity. But the preparation process is time-consuming, complicated, and will make the catalytic layer thicker, and lead to sizeable internal resistance and catalyst falling off.

The soaking-drying method in this work can easily achieve the gradient distribution of hydrophobic materials. When dropping 3 mL deionized water (DIW) drops on the front and backside of an electrode after waterproof treatment (MnO<sub>2</sub> × 2/NiF-PTFE-1), respectively, the different contact angles of the two surfaces is observed. The DIW drops on the front side of the electrode cannot be maintained (Fig. 4a), which elucidates there is barely any PTFE on this side. The backside of the electrode represents a high hydrophobicity (Fig. 4b), on which the DIW drops can polymerize into beads, which illustrates that gradient hydrophobicity can be achieved on two sides of the same electrode though one waterproof treatment. The gradient distribution of hydrophobic materials on both sides of the air cathode results in different hydrophobicity of the two surfaces. Hydrophilic surfaces are used to provide access to aqueous electrolytes. Hydrophobic surfaces are designed to provide a barrier to prevent electrolyte penetration and to facilitate the rapid diffusion of oxygen from the atmosphere to catalytic sites. Therefore, the gradient hydrophobicity of air electrode is helpful to slow down the loss of water evaporation or resist flooding under extreme

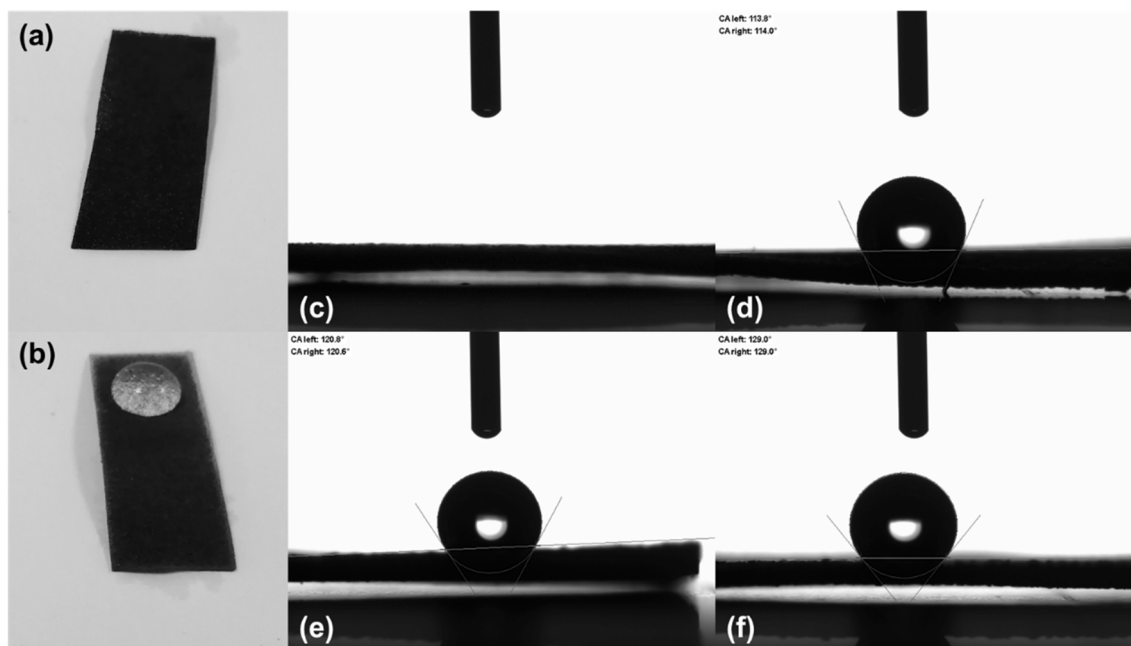


**Fig 4.** The surface hydrophobicity of a (a) downward facing surface and a (b) upward facing surface after a 3 mL deionized water drop onto the surface. Contact angles of DIW droplets on the backside of different  $\text{MnO}_2/\text{NiF}$  surfaces. (c) The pristine electrode ( $\text{MnO}_2/\text{NiF} \times 2\text{-PTFE-0}$ ). (d-f) The electrodes with different PTFE loadings: (d)  $\text{MnO}_2/\text{NiF} \times 2\text{-PTFE-1}$ , (e)  $\text{MnO}_2/\text{NiF} \times 2\text{-PTFE-2}$ , and (f)  $\text{MnO}_2/\text{NiF} \times 2\text{-PTFE-3}$ .

conditions [40,41].

In addition, the non-uniform distribution of hydrophobic materials on both sides of the air cathode is conducive to efficient oxygen transport, thus promoting the formation of three-phase reaction interface [39,42]. To investigate the effect of PTFE on the hydrophobicity, we

measured the contact angles of DIW drops on the backside of different  $\text{MnO}_2/\text{NiF}$  surfaces. For the pristine electrode without waterproof treatment ( $\text{MnO}_2/\text{NiF} \times 2\text{-PTFE-0}$ ), the DIW drops are quickly absorbed into the macropores of the pieces (Fig. 4c), demonstrating the high hydrophilicity. After waterproof treatment with PTFE, including one

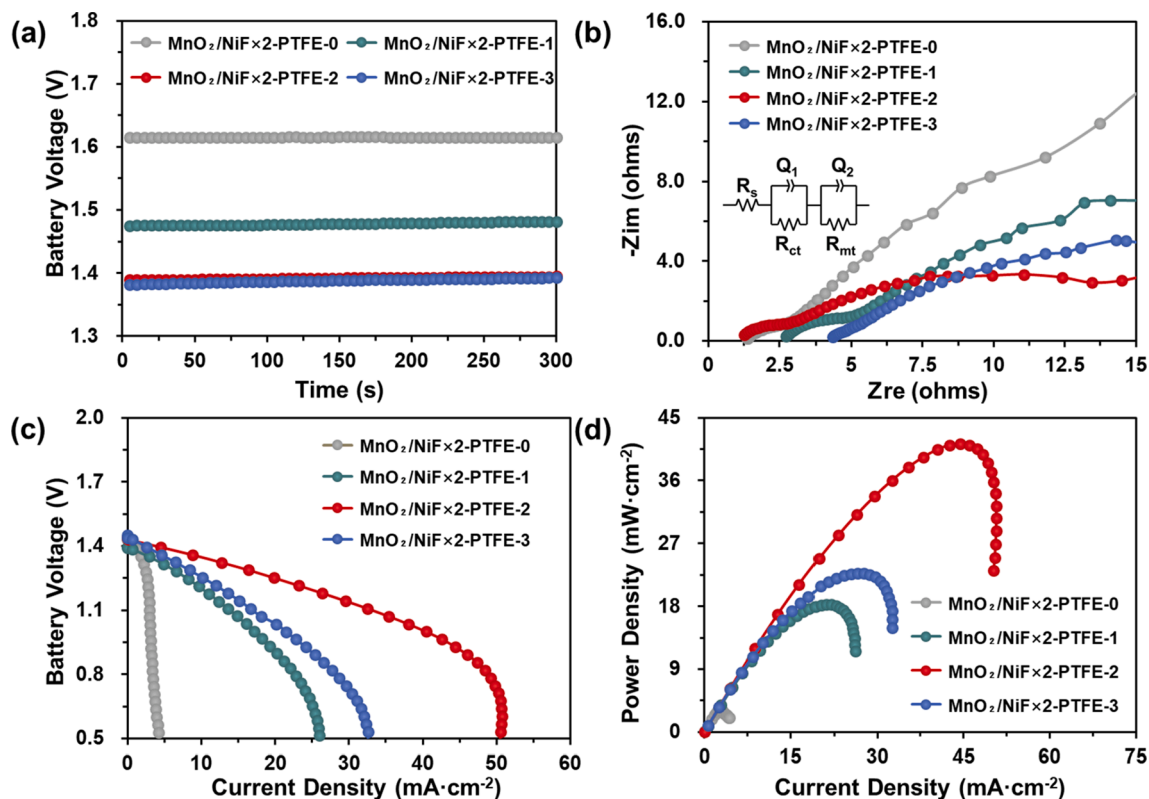


**Fig 5.** The electrochemical performance of zinc-air batteries assembled by air cathodes of  $\text{MnO}_2/\text{NiF} \times 2$  with different hydrophobicity. (a) Open-circuit voltage curve. (b) Electrochemical impedance spectroscopy recorded at a constant discharge potential of 1 V. The profiles of (c) Galvano dynamic discharge voltage and (d) corresponding power densities.

soaking-drying process ( $\text{MnO}_2/\text{NiF} \times 2\text{-PTFE-1}$ ), the contact angle increases to  $113.9^\circ$  on average (Fig. 4d). When expanding the treatment of the soaking-drying process to two ( $\text{MnO}_2/\text{NiF} \times 2\text{-PTFE-2}$ ) or three times ( $\text{MnO}_2/\text{NiF} \times 2\text{-PTFE-3}$ ), the contact angles are up to  $120.7^\circ$  and  $129.0^\circ$  in average (Fig. 4e, f), which indicates that the PTFE loading can improve the hydrophobicity of the backside of the electrode. It is noteworthy that the front side of the electrode maintains hydrophilicity because PTFE mainly deposits on the other side during waterproof treatment. Hence, the gradient hydrophobicity in different degrees is achieved [30].

The electrochemical performance of the air cathodes with hydrophobicity in different hydrophobicity is shown in Fig. 5. The open circuit voltages (Fig. 5a) of different electrodes are significant heterogeneity. The electrode without waterproof treatment ( $\text{MnO}_2/\text{NiF} \times 2\text{-PTFE-0}$ ) illustrates a stable open circuit voltage at about 1.62 V, which is closer to the typical open circuit voltage of zinc manganese battery at 1.5–1.8 V [43–45]. There is no PTFE loading on the electrode, so it is difficult for  $\text{O}_2$  to transfer through GDL and into the catalytic layer. The electrochemical system with zinc and manganese oxide immersed in the electrolyte is near zinc manganese battery. Increasing PTFE loading on the electrode by one time soaking-drying process ( $\text{MnO}_2/\text{NiF} \times 2\text{-PTFE-1}$ ), the result illustrates at 1.48 V, which is close to the reported zinc-air batteries [46]. When the soaking-drying process reaches twice or more ( $\text{MnO}_2/\text{NiF} \times 2\text{-PTFE-2}$ ,  $\text{MnO}_2/\text{NiF} \times 2\text{-PTFE-3}$ ), the open circuit voltages are almost the same at around 1.40 V, which are the typical open circuit voltage in zinc-air batteries [14,47,48], indicating that a sufficient PTFE loading can ensure the electrochemical system a stable zinc-air battery, avoiding the formation of zinc-manganese battery or zinc hybrid battery. In addition to electrochemical properties, electrochemical impedance spectroscopy (EIS) analysis results (Fig. 5b) elucidate that surface hydrophobicity with a suitable composition of PTFE significantly reduces the impedance of mass and charge transfer.

The Nyquist plots consist of two semicircles. One in high frequency is for kinetic control process, and the other in low frequency is for mass transfer control. The EIS data are fitted using an electrical equivalent circuit model of which the circuit description code is  $R_s((R_{ct}Q_1)(R_{mt}Q_2))$ , as shown in Fig. 5b. The details are shown in Table 1. To qualitatively analyze, the air cathode with high PTFE loading illustrates lower electrolyte, contact, and solid-electrolyte interface resistances but higher mass transfer resistances. Meanwhile, opposite characteristics can be revealed in air cathodes with low PTFE loading, which means that a suitable composition of PTFE ( $\text{MnO}_2/\text{NiF} \times 2\text{-PTFE-2}$ ) can achieve the balance of mass transfer and charge transfer. In the discharge voltage polarization and power density curves (Fig. 5c, 5d), it is also found.

When the current density increases to  $4.29 \text{ mA}\cdot\text{cm}^{-2}$ , the voltage quickly drops below 0.5 V for the pristine electrode, which is consistent with the former reports that the power density of zinc manganese batteries is lower than that of zinc-air batteries. The peak power density of the batteries with different electrodes ( $\text{MnO}_2/\text{NiF} \times 2\text{-PTFE-0}$ ,  $\text{MnO}_2/\text{NiF} \times 2\text{-PTFE-1}$  and  $\text{MnO}_2/\text{NiF} \times 2\text{-PTFE-2}$ ) reach  $4.0 \text{ mW}\cdot\text{cm}^{-2}$ ,  $17.0 \text{ mW}\cdot\text{cm}^{-2}$ , and  $40.0 \text{ mW}\cdot\text{cm}^{-2}$ , respectively. When the soaking-drying process reaches twice or more, the battery has the open circuit voltage

**Table 1**

Values of equivalent circuit elements based on EIS analysis of  $\text{MnO}_2/\text{NiF}$  electrodes with different PTFE loading.

Element	$R_s$ ( $\Omega\cdot\text{cm}^2$ )	$R_{ct}$ ( $\Omega\cdot\text{cm}^2$ )	$R_{mt}$ ( $\Omega\cdot\text{cm}^2$ )	$Q_1$ (S-sn)	$Q_2$ (S-sn)
$\text{MnO}_2/\text{NiF} \times 2\text{-PTFE-0}$	1.30	1.53	62.2	$2.93 \times 10^{-3}$	0.0152
$\text{MnO}_2/\text{NiF} \times 2\text{-PTFE-1}$	2.62	1.83	41.8	$8.87 \times 10^{-4}$	0.0190
$\text{MnO}_2/\text{NiF} \times 2\text{-PTFE-2}$	1.07	1.50	19.5	$6.85 \times 10^{-4}$	0.0149
$\text{MnO}_2/\text{NiF} \times 2\text{-PTFE-3}$	4.09	3.11	43.3	0.0135	0.0329

of the zinc-air battery reported in the general report. However, the power output of zinc-air batteries will be negatively affected by the excessive load of PTFE. Compared with the optimal  $\text{MnO}_2/\text{NiF} \times 2\text{-PTFE-2}$ , the discharge voltage (Fig. 5c) and power density (Fig. 5d) of  $\text{MnO}_2/\text{NiF} \times 2\text{-PTFE-3}$  with increasing hydrophobicity gradually decreased. There are two main reasons for the rapid decline of power output performance with high hydrophobicity of the air cathode. On the one hand, the increased hydrophobicity of the air cathode limits the transfer of electrolyte that can enter the catalytic layer, and the gas–solid interfaces become predominant in the three-phase reaction interfaces. On the other hand, the air cathode with high hydrophobicity is loaded with too much non-conductive PTFE, and the excess PTFE will cover the pores of the catalyst layer and nickel framework, and the effective area of catalyst exposed in the three-phase reaction interfaces is reduced. The highest discharge voltage and power density plateau pertain to a moderately hydrophobic electrode with the optimum PTFE loading when the soaking-drying process reaches twice, which is similar to the reported results [29,30]. Therefore, the moderate PTFE loading can not only keep the balance between the hydrophobicity and hydrophilicity in the novel structure, but also reduce mass transfer and charge transfer impedance to make high power density for zinc-air batteries.

### 3.3. Effect of multi current collectors on battery performance

In the air cathode, the direct growth catalysts on current collectors avoid the active materials falling off and increasing the internal resistance during charge and discharge cycling. For low-cost transition metal oxides, an increase in the amount of catalyst to increase the reaction rate on the cathode side is generally allowed. However, even without considering the high cost of catalysts, it is difficult to enhance electrocatalytic kinetics by growing more catalysts on a single current collector, making the catalytic layer thicker. The impedance of electron transfer is higher in the thicker catalytic layer. Furthermore, the macropores between the current collector framework will be blocked by catalysts, making the transport of electrolyte and air unsmooth, which is disastrous for constructing three-phase reaction interfaces.

To avoid the above problems and increase the deposition of catalysts, we propose a novel air cathode structure with multiple current collectors. It is predicted that the increase in the number of current collectors will not only expand the catalytic reaction area but also control the growth of internal electrode resistance and the loss of catalysts.

The effect of multi current collectors are revealed by discrepant performance between air cathodes with different amount of  $\text{MnO}_2/\text{NiF}$ . The open circuit voltages are around 1.38–1.43 V (Fig. 6a) because their soaking-drying process reaches twice. They are all stable electrochemical systems of zinc-air batteries. The significant reduction of impedance using multi current collectors to substitute for a single current collector (Fig. 6b). With increasing the number of current collectors from 1 to 5, the ohmic resistance, mass transfer resistance, and charge transfer resistance all decrease rapidly (Table.2). Because the catalyst deposited later grows directly on the nickel foam, it will not cause an immensely negative effect on the transfer of electrons and oxygen. Also, adopting a novel air cathode structure can improve the discharge voltage and increase the discharge power density (Fig. 6c, d). When the electrode contains one piece of  $\text{MnO}_2/\text{NiF}$ , the voltage of the zinc-air battery drops below 0.4 V at the current density of  $23.5 \text{ mA}\cdot\text{cm}^{-2}$ . After doubling the  $\text{MnO}_2/\text{NiF}$  pieces, the current density rises to  $49.9 \text{ mA}\cdot\text{cm}^{-2}$  at the same voltage. Furthermore, the battery with 5 pieces of  $\text{MnO}_2/\text{NiF}$  can work under  $246 \text{ mA}\cdot\text{cm}^{-2}$ , 0.38 V in which other samples cease to be effective, revealing that multi current collectors all promote the discharge current output. Similarly, the reply incremental power densities are shown in Fig. 6d. When the number of  $\text{MnO}_2/\text{NiF}$  pieces is further increased to 6, the peak power density of zinc air battery is only  $99 \text{ mW}\cdot\text{cm}^{-2}$  (Fig. 6d). It is considered that the thickness of air cathode is too large, which results in the increase of mass transfer impedance (Fig. 6b, Table.2). The oxygen passing through the microchannel to the

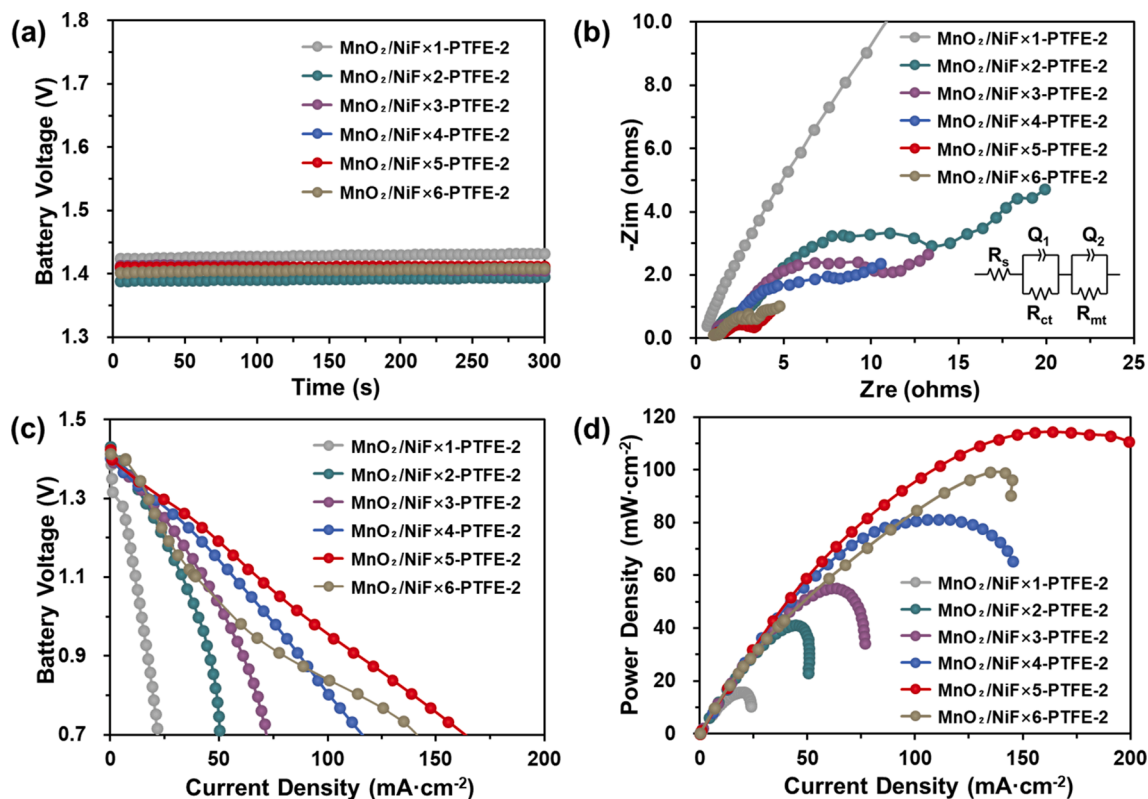


**Fig. 6.** The electrochemical performance of zinc-air batteries assembled by air cathodes of  $\text{MnO}_2/\text{NiF}$  with different amounts of current collectors. (a) Open-circuit voltage curve. (b) Electrochemical impedance spectroscopy recorded at a constant discharge potential of 1 V. The profiles of (c) Galvanostatic discharge voltage and (d) corresponding power density.

**Table 2**

Values of equivalent circuit elements based on EIS analysis of  $\text{MnO}_2/\text{NiF}$  electrodes with different number of current collectors.

Element	$R_s$ ( $\Omega\text{-cm}^2$ )	$R_{ct}$ ( $\Omega\text{-cm}^2$ )	$R_{mt}$ ( $\Omega\text{-cm}^2$ )	$Q_1$ (S-sn)	$Q_2$ (S-sn)
$\text{MnO}_2/\text{NiF} \times 1$ -PTFE-2	0.316	9.23	431	$3.62 \times 10^{-3}$	$4.72 \times 10^{-3}$
$\text{MnO}_2/\text{NiF} \times 2$ -PTFE-2	1.07	1.50	19.5	$6.85 \times 10^{-4}$	0.0149
$\text{MnO}_2/\text{NiF} \times 3$ -PTFE-2	0.802	1.41	11.4	$2.09 \times 10^{-3}$	0.0169
$\text{MnO}_2/\text{NiF} \times 4$ -PTFE-2	0.574	2.20	8.33	0.0457	0.0238
$\text{MnO}_2/\text{NiF} \times 5$ -PTFE-2	1.02	0.834	2.54	0.0230	0.111
$\text{MnO}_2/\text{NiF} \times 6$ -PTFE-2	0.419	0.830	4.63	0.0120	0.120

inside of the cell encounters greater resistance, which makes the formation of three-phase reaction interface difficult, and some catalysts are not effectively utilized.

With the increase in the number of  $\text{MnO}_2/\text{NiF}$  in the air cathode, the peak power density of the zinc-air battery is approximately linearly magnified (Fig. 7a). When the number of a collector is five, the peak power density reaches  $114.3 \text{ mW}\cdot\text{cm}^{-2}$ . The thickness of the air cathode is increased to 1.5 mm by five collectors. Further thickening of the cathode will lead to an increase of internal impedance, so this is considered to be a better acceptable limit. Based on the novel structure of the air cathode prepared by the in-situ growth of catalyst on current collectors, the problem of large impedance caused by catalyst deposition can be alleviated.

In the previous experiment, the air cathode ( $\text{MnO}_2/\text{NiF} \times 5$ -PTFE-2) with moderate PTFE loading and 5 pieces of current collectors is

considered to achieve the highest discharge voltage and power in the zinc-air battery. As shown in Fig. 7b, we further study the continuous working performance under a constant discharge current density at  $20 \text{ mA}\cdot\text{cm}^{-2}$  with this air cathode. In the first 5 h, the battery keeps a discharge voltage of about 1.08 V, of which the power density is around  $21.6 \text{ mW}\cdot\text{cm}^{-2}$ . The discharge voltage of the battery continues to drop after 5 h of continuous discharge. Another 1 h later, the discharge voltage drops below 1.00 V. When the battery operates continuously for 9.5 h without replacing any active materials, the battery voltage is lower than 0.05 V. This indicates that the battery has completely degraded. It does not ascribe to the failure of the air cathode but the consumption of anode materials. We disassembled the battery and found that the effective area of zinc foil had been completely consumed (Fig. 7c). Replaced the consumed sample with a new zinc foil as the anode, keep the original air cathode as a cathode, other components and battery structure unchanged, and tested again. The results elucidate that the scanning curves of voltage and power density of the new battery are almost identical with those of the initial battery. The peak power density of zinc-air battery equipped with the same air cathode is maintained at  $110\text{--}120 \text{ mW}\cdot\text{cm}^{-2}$ , as shown in Fig. 7d, which means that the decrease of the effective reaction area of anode is the reason of the continuous voltage decay after long-term discharge. The air cathode has no apparent change. After changing the anode material, the battery can recover its original discharge capacity.

It is worth noting that although the power density and specific power of zinc air battery are important performance evaluation indexes, there are obvious differences between them [14,49,50]. The power density is the ratio of the battery power to the air cathode active surface. The specific power is the ratio of the battery power to the overall mass. The overall quality of the battery is affected by the overall structure design, anode materials and other comprehensive factors. In order to evaluate the effect of air cathode structure design, it is appropriate to use power

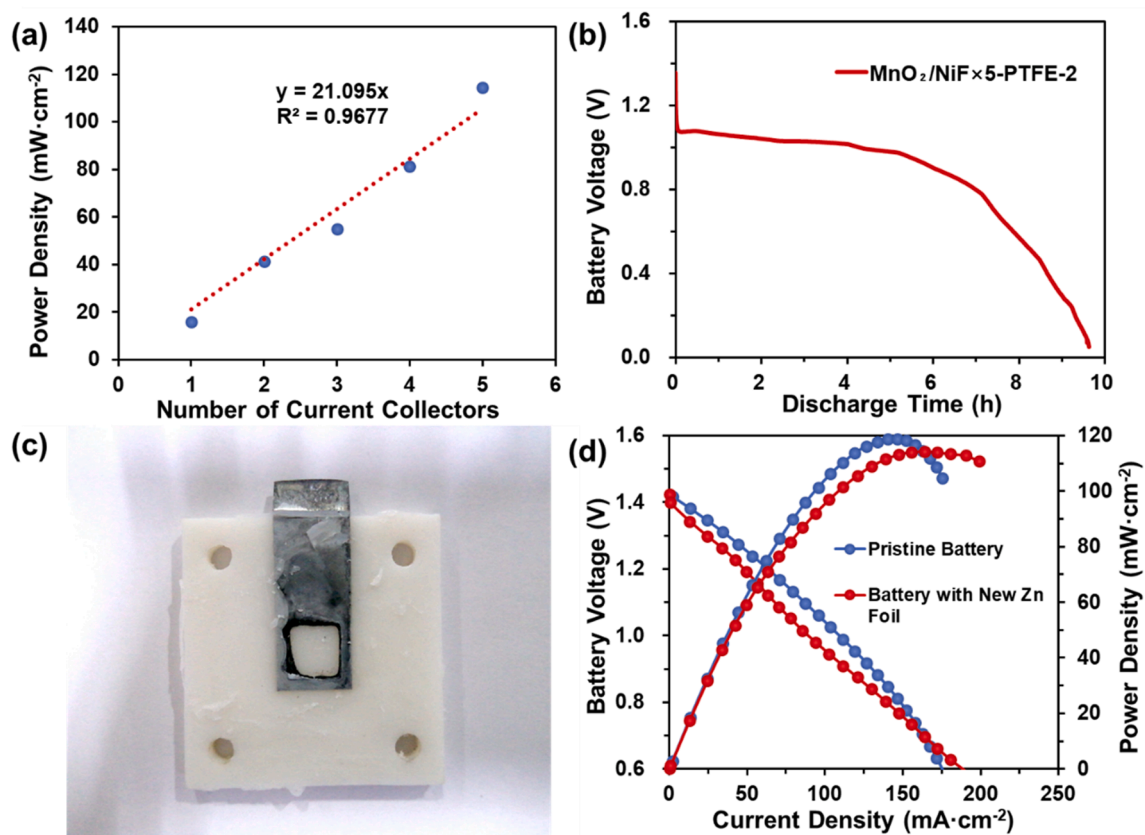


**Fig 7.** The electrochemical performance of zinc-air batteries assembled by air cathodes of  $\text{MnO}_2/\text{NiF} \times 5\text{-PTFE-2}$ . (a) The fitting curve of the number of current collectors and peak power density. (b) The voltage curve of continuous discharging at  $20 \text{ mA}\cdot\text{cm}^{-2}$ . (c) The active region of the zinc foil has been completely consumed. (d) Discharge voltage and power density curve before and after anode replacement.

density as the key performance evaluation index. Using  $\text{MnO}_2$  as catalyst, the novel air cathode structural design can significantly improve the power density of zinc air battery compared with conventional structure as reported (Table.3). This means that the output power of zinc air battery can be improved through the new structural design with a low catalysts loading.

#### 4. Conclusions

For the issues of air cathode structure, a novel structural design with

multiple current collectors is proposed. The feasibility of this novel structure for increasing the discharge power density of zinc-air batteries is verified. By adjusting the surface hydrophobicity, changing the number of current collectors, and replacing the anode material, the following conclusions can be drawn.

- (1) The hydrophobic gradient distribution through air cathodes can be obtained quickly by the soaking-drying process. When the soaking-drying process reaches twice, the zinc-air battery can

**Table 3**

Comparison of electrochemistry performance of zinc-air batteries with air cathodes in reported conventional structure and novel structure.

Catalysts	Anode	Catalysts Loading ( $\text{mg}\cdot\text{cm}^{-2}$ )	Electrolyte	Peak Power Density ( $\text{mW}\cdot\text{cm}^{-2}$ )	Power Density Per Catalysts Loading ( $\text{mW}\cdot\text{mg}^{-1}$ )	Reference
$\text{MnO}_x$	Zinc plate (4.5 g)	40 (with carbon)	6 M KOH	38.5	7.13	[51]
$\alpha\text{-MnO}_2$	Zinc foil	6.25 (with carbon)	6 M KOH	61.5	9.84	[52]
$\alpha\text{-MnO}_2$	Zinc foil	10	6 M KOH	176	17.6	[53]
$\text{MnO}_2$	Zinc plate	4	6 M KOH	95.7	23.9	[31]
$\text{MnO}_2$	Zinc plate	~ 1	6 M KOH	48	48	[54]
			20 $\text{g}\cdot\text{L}^{-1}$ Zn (AC) <sub>2</sub>			
$\text{MnO}_2$	Zinc plate	3	6 M KOH	151	50.3	[55]
$\text{MnO}_2$	Zinc plate (~0.5 mm)	2	0.2 M Zn(AC) <sub>2</sub>	105	52.5	[56]
$\alpha\text{-MnO}_2$	Zinc plate	~2	6 M KOH	166	83	[46]
$\alpha\text{-MnO}_2$	Zinc plate	~1.25 (with carbon)	6 M KOH	116	92.8	[57]
$\delta\text{-MnO}_2$	Zinc plate (~0.2 mm)	1	0.15 M ZnO	120	120	This Work
			6 M KOH			
			0.2 M ZnO			

balance mass transfer and charge transfer impedance and achieve the highest discharge power density.

- (2) Using the proposed air cathode structure, the peak power density of zinc-air batteries approximately linearly increases by directly assembling more current collectors in the air cathode. The zinc-air battery with 5 pieces of  $\text{MnO}_2/\text{NiF}$  represents a peak power density of  $120 \text{ mW}\cdot\text{cm}^{-2}$ .
- (3) After continuous discharging for more than 9 h, the performance of the air cathode does not decline obviously. The discharge voltage and power density of the zinc-air battery can be restored to the performance before discharge after replacing a new anode with the same material.

In addition, based on the results of this paper, the new air cathode structure can be used in combination with other catalysts and metal-air batteries, so as to expand the three-phase reaction interface into three-dimensional space and achieve higher voltage and power. This will promote the commercial application of zinc air battery, especially in the fields of backup energy, power system and wearable devices.

#### CRedit authorship contribution statement

**Lyuming Pan:** Conceptualization, Methodology, Writing - original draft. **Dongfang Chen:** Data curation, Writing - review & editing. **Pucheng Pei:** Supervision. **Shangwei Huang:** Visualization. **Peng Ren:** Software, Investigation. **Xin Song:** Software.

#### Declaration of Competing Interest

The authors declare that they have no known competing financial interests or personal relationships that could have appeared to influence the work reported in this paper.

#### Acknowledgments

This work is funded by the National Key Research and Development Program of China (Nos.2017YFB0102705 and 2016YFB0101305) and National Natural Science Foundation of China (Nos.21975143 and 21676158).

#### References

- [1] Chu S, Majumdar A. Opportunities and challenges for a sustainable energy future. *Nature* 2012;488:294–303.
- [2] Armand M, Tarascon JM. Building better batteries. *Nature* 2008;451:652–7.
- [3] Cano ZP, Banham D, Ye SY, Hintennach A, Lu J, Fowler M, et al. Batteries and fuel cells for emerging electric vehicle markets. *Nat Energy* 2018;3:279–89.
- [4] Pei PC, Wang KL, Ma Z. Technologies for extending zinc-air battery's cyclelife: A review. *Appl Energy* 2014;128:315–24.
- [5] Fu J, Cano ZP, Park MG, Yu AP, Fowler M, Chen ZW. Electrically rechargeable zinc-air batteries: progress, challenges, and perspectives. *Adv Mater* 2017;29:34.
- [6] Wang KL, Liu XT, Pei PC, Xiao Y, Wang YC. Guiding bubble motion of rechargeable zinc-air battery with electromagnetic force. *Chem Eng J* 2018;352:182–7.
- [7] Han G, Kwon Y, Kim JB, Lee S, Bae J, Cho E, et al. Development of a high-energy-density portable/mobile hydrogen energy storage system incorporating an electrolyzer, a metal hydride and a fuel cell. *Appl Energy* 2020;259:12.
- [8] Chen XC, Zhou Z, Karahan HE, Shao Q, Wei L, Chen Y. Recent advances in materials and design of electrochemically rechargeable zinc-air batteries. *Small* 2018;14:29.
- [9] Yuan RH, He Y, He W, Ni M, Leung MKH. Bifunctional electrocatalytic activity of  $\text{La}_0.8\text{Sr}_0.2\text{MnO}_3$ -based perovskite with the A-site deficiency for oxygen reduction and evolution reactions in alkaline media. *Appl Energy* 2019;251:10.
- [10] She YY, Chen JF, Zhang CX, Lu ZG, Ni M, Sit PHL, et al. Nitrogen-doped graphene derived from ionic liquid as metal-free catalyst for oxygen reduction reaction and its mechanisms. *Appl Energy* 2018;225:513–21.
- [11] Wang LK, Bliznakov S, Isseroff R, Zhou YC, Zuo XH, Raut A, et al. Enhancing proton exchange membrane fuel cell performance via graphene oxide surface synergy. *Appl Energy* 2020;261:7.
- [12] Wang KL. Solutions for dendrite growth of electrodeposited zinc. *ACS Omega* 2020; 5:10225–7.
- [13] Huang S, Li H, Pei P, Wang K, Xiao Y, Zhang C, et al. A dendrite-resistant zinc-air battery. *iScience* 2020;23:101169.

- [14] Pei PC, Huang SW, Chen DF, Li YH, Wu ZY, Ren P, et al. A high-energy-density and long-stable-performance zinc-air fuel cell system. *Appl Energy* 2019;241:124–9.
- [15] Seh ZW, Kibsgaard J, Dickens CF, Chorkendorff IB, Norskov JK, Jaramillo TF. Combining theory and experiment in electrocatalysis: Insights into materials design. *Science* 2017;355:1.
- [16] Wang YJ, Long WY, Wang LL, Yuan RS, Ignaszak A, Fang BZ, et al. Unlocking the door to highly active ORR catalysts for PEMFC applications: polyhedron-engineered Pt-based nanocrystals. *Energ Environ Sci* 2018;11:258–75.
- [17] Suntivich J, May KJ, Gasteiger HA, Goodenough JB, Shao-Horn Y. A perovskite oxide optimized for oxygen evolution catalysis from molecular orbital principles. *Science* 2011;334:1383–5.
- [18] Wu MJ, Zhang GX, Wu MH, Prakash J, Sun SH. Rational design of multifunctional air electrodes for rechargeable Zn-Air batteries: Recent progress and future perspectives. *Energy Storage Mater* 2019;21:253–86.
- [19] Wang KL, Pei PC, Wang YC, Liao C, Wang W, Huang SW. Advanced rechargeable zinc-air battery with parameter optimization. *Appl Energy* 2018;225:848–56.
- [20] Cai XY, Lai LF, Lin JY, Shen ZX. Recent advances in air electrodes for Zn-air batteries: electrocatalysis and structural design. *Mater Horiz* 2017;4:945–76.
- [21] Wang KL, Yu JR. Lifetime simulation of rechargeable zinc-air battery based on electrode aging. *J Energy Storage* 2020;28:8.
- [22] Wang KL, Liao C, Wang W, Xiao Y, Liu XT, Zhao SY. Physical shortcut accelerating electron transport of rechargeable zinc-air battery. *Mater Today Energy* 2019;14:6.
- [23] Wang HF, Tang C, Zhang Q. A review of precious-metal-free bifunctional oxygen electrocatalysts: rational design and applications in Zn-air batteries. *Adv Funct Mater* 2018;28:22.
- [24] Neburchilov V, Wang HJ, Martin JJ, Qu W. A review on air cathodes for zinc-air fuel cells. *J Power Sources* 2010;195:1271–91.
- [25] Mohideen MM, Liu Y, Ramakrishna S. Recent progress of carbon dots and carbon nanotubes applied in oxygen reduction reaction of fuel cell for transportation. *Appl Energy* 2020;257:19.
- [26] Hou YZ, Deng H, Pan FW, Chen WM, Du Q, Jiao K. Pore-scale investigation of catalyst layer ingredient and structure effect in proton exchange membrane fuel cell. *Appl Energy* 2019;253:10.
- [27] Xu N, Zhang Y, Wang Y, Wang M, Su T, Coco CA, et al. Hierarchical bifunctional catalysts with tailored catalytic activity for high-energy rechargeable Zn-air batteries. *Appl Energy* 2020;279.
- [28] Yang DJ, Zhang LJ, Yan XC, Yao XD. Recent progress in oxygen electrocatalysts for zinc-air batteries. *Small Methods* 2017;1:16.
- [29] Chen M, Jiang XL, Yang H, Shen PK. Performance improvement of air electrode for Li/Air batteries by hydrophobicity adjustment. *J Mater Chem A* 2015;3:11874–9.
- [30] Tan P, Chen B, Xu HR, Cai WZ, He W, Ni M. Investigation on the electrode design of hybrid  $\text{Zn-Co}_3\text{O}_4$ /air batteries for performance improvements. *Electrochim Acta* 2018;283:1028–36.
- [31] Xu K, Loh A, Wang BG, Li XH. Enhancement of oxygen transfer by design nickel foam electrode for zinc-air battery. *J Electrochem Soc* 2018;165:A809–18.
- [32] Zhao YX, Chang C, Teng F, Zhao YF, Chen GB, Shi R, et al. Defect-engineered ultrathin  $\delta\text{-MnO}_2$  nanosheet arrays as bifunctional electrodes for efficient overall water splitting. *Adv Energy Mater* 2017;7:7.
- [33] Xu NN, Liu JW, Qiao JL, Huang HT, Zhou XD. Interweaving between  $\text{MnO}_2$  nanowires/nanorods and carbon nanotubes as robust multifunctional electrode for both liquid and flexible electrochemical energy devices. *J Power Sources* 2020; 455:10.
- [34] Mathur A, Kaushik R, Halder A. Visible-light-driven photo-enhanced zinc-air batteries using synergistic effect of different types of  $\text{MnO}_2$  nanostructures. *Catal Sci Technol* 2020;10:7352–64.
- [35] Meng YT, Song WQ, Huang H, Ren Z, Chen SY, Suib SL. Structure-property relationship of bifunctional  $\text{MnO}_2$  nanostructures: highly efficient, ultra-stable electrochemical water oxidation and oxygen reduction reaction catalysts identified in alkaline media. *J Am Chem Soc* 2014;136:11452–64.
- [36] Xu K, Song J, Song P, Xu G, Deng Z. Performance decay of air electrode configuration for rechargeable zinc-air batteries. *J Electrochem Soc* 2020;167.
- [37] Cheng FY, Zhang TR, Zhang Y, Du J, Han XP, Chen J. Enhancing electrocatalytic oxygen reduction on  $\text{MnO}_2$  with vacancies. *Angew Chem-Int Edit* 2013;52:2474–7.
- [38] Loh AL, Xu K, Li XH, Wang BG. Influence of synthesis parameters on amorphous manganese dioxide catalyst electrocatalytic performance. *Electrochim Acta* 2017; 245:615–24.
- [39] Tan P, Shyy W, An L, Wei ZH, Zhao TS. A gradient porous cathode for non-aqueous lithium-air batteries leading to a high capacity. *Electrochem Commun* 2014;46: 111–4.
- [40] Li YG, Dai HJ. Recent advances in zinc-air batteries. *Chem Soc Rev* 2014;43: 5257–75.
- [41] Ugalde AR, Naguib HE. Double-layer membrane cathode with improved oxygen diffusivity in zinc air batteries. *Energy Storage Mater* 2017;8:1–9.
- [42] Zhang NY, Deng CW, Tao S, Guo LB, Cheng YH. Bifunctional oxygen electrodes with gradient hydrophilic/hydrophobic reactive interfaces for metal air flow batteries. *Chem Eng Sci* 2020;224:7.
- [43] Zhong C, Liu B, Ding J, Liu XR, Zhong YW, Li Y, et al. Decoupling electrolytes towards stable and high-energy rechargeable aqueous zinc-manganese dioxide batteries. *Nat Energy* 2020;5:440–9.
- [44] Minakshi M, Singh P, Issa TB, Thurgate S, De Marco R. Lithium insertion into manganese dioxide electrode in  $\text{MnO}_2/\text{Zn}$  aqueous battery Part II. Comparison of the behavior of EMD and battery grade  $\text{MnO}_2$  in Zn vertical bar  $\text{MnO}_2$  vertical bar aqueous LiOH electrolyte. *J Power Sources* 2004;138:319–22.
- [45] Nuanwat W, Pattananuwat P. Preparation of polypyrrole coated zinc anode electrode for inhibition corrosion of secondary zinc ion battery. *IOP Conf Ser: Mater Sci Eng* 2019;600. 012002(5 pp.).

- [46] Gu YD, Yan GB, Lian YB, Qi PW, Mu QQ, Zhang CF, et al. Mn-III-enriched alpha-MnO<sub>2</sub> nanowires as efficient bifunctional oxygen catalysts for rechargeable Zn-air batteries. *Energy Storage Mater* 2019;23:252–60.
- [47] Wang KL, Pei PC, Wang YC. Magnetic field improving interfacial behavior of the two-electrode system. *J Electrochem Soc* 2017;164:A3440–4.
- [48] Wang KL, Xiao Y, Pei PC, Liu XT, Wang YC. A phase-field model of dendrite growth of electrodeposited zinc. *J Electrochem Soc* 2019;166:D389–94.
- [49] Cai PW, Li Y, Chen JX, Jia JC, Wang GX, Wen ZH. An asymmetric-electrolyte Zn-air battery with ultrahigh power density and energy density. *Chemelectrochem* 2018; 5:589–92.
- [50] Mehta MR, Knudsen KB, Bennett WR, McCloskey BD, Lawson JW. Li-O-2 batteries for high specific power applications: A multiphysics simulation study for a single discharge. *J Power Sources* 2021;484.
- [51] Rao CS, Gunasekaran G. Cobalt-Lead-Manganese oxides combined cathode catalyst for air electrode in Zinc -air battery. *Electrochim Acta* 2015;176:649–56.
- [52] Li PC, Hu CC, Noda H, Habazaki H. Synthesis and characterization of carbon black/manganese oxide air cathodes for zinc-air batteries: Effects of the crystalline structure of manganese oxides. *J Power Sources* 2015;298:102–13.
- [53] Meng J, Liu FM, Yan ZH, Cheng FY, Li FJ, Chen J. Spent alkaline battery-derived manganese oxides as efficient oxygen electrocatalysts for Zn-air batteries. *Inorg Chem Front* 2018;5:2167–73.
- [54] Sumboja A, Ge XM, Goh FWT, Li B, Geng DS, Hor TSA, et al. Manganese oxide catalyst grown on carbon paper as an air cathode for high-performance rechargeable zinc-air batteries. *Chempluschem* 2015;80:1341–6.
- [55] Zhong Y, Dai J, Xu X, Su C, Shao Z. Facilitating oxygen redox on manganese oxide nanosheets by tuning active species and oxygen defects for zinc-air batteries. *Chemelectrochem* 2020;7:4949–55.
- [56] Xu NN, Cai YX, Peng LW, Qiao JL, Wang YD, Chirdon WM, et al. Superior stability of a bifunctional oxygen electrode for primary, rechargeable and flexible Zn-air batteries. *Nanoscale* 2018;10:13626–37.
- [57] Marsudi MA, Ma YY, Prakoso B, Hutani JJ, Wibowo A, Zong Y, et al. Manganese oxide nanorods decorated table sugar derived carbon as efficient bifunctional catalyst in rechargeable Zn-air batteries. *Catalysts* 2020;10:11.